Improvement of the Fatigue Life of an Electron-Beam Welded Ti_2AlNb Joint subjected to an Electromagnetic Coupling Treatment

Qiang Li [a,b], Xiaotong Wang [c], Yi Qin [d], Kunlan Huang [a,b,*], Jie Wang [a,b]

[a] *School of Mechanical Engineering, Sichuan University, Chengdu 610065, PR China*

[b] *Yibin Institute of Industrial Technology, Sichuan University Yibin Park, Yibin 644000, PR China*

[c] *Aeroengine Research Institute, Beihang University, Beijing 100191, PR China*

[d] *Centre for Precision Manufacturing, DMEM, The University of Strathclyde, James Weir Building, 75 Montrose Street, Glasgow G1 1XJ, UK*

(*) Corresponding Author: Kunlan Huang, E-Mail: huangkunlan@scu.edu.cn.

Abstract: The local stress concentration created by the seam welding process often reduces the fatigue life of the material along and around the seam. Post-welding heat treatment is usually used to improve the weld performance, but the improvement effect on fatigue life may not be obvious. In this study, a new treatment method of electromagnetic coupling was applied to regulate the Ti_2AlNb electron beam weld after heat treatment, so as to improve the fatigue properties of the welded joint. The results show that after electromagnetic coupling treatment, the fatigue limit of the welded joint is increased by 10.4%, the residual compressive stress is increased, and the fatigue crack propagation rate is decreased. The microstructure analysis shows that after electromagnetic coupling treatment, the fatigue crack source starts in the subsurface layer, the substructural crystals in the fusion zone and the heat affected zone decrease, the recrystallization content and the large angle grain boundary increase, and the dislocation density increases and tends to be homogenized. Local high density dislocation is found in the grain, which causes dislocation entanglement and hinders crack initiation and propagation and this provides an important basis for improving fatigue properties. This study provides a new method for improving the fatigue properties of Ti_2AlNb electron beam welds which can also be used to study the properties of other welded joints.

Key words: Electromagnetic Coupling Treatment; Ti_2AlNb; Electron Beam Welding; Fatigue Life

Nomenclature	Full name
EBW	Electron Beam Welding
PWHT	Post-Weld Heat Treatment
UT	Untreated
PET	Pulsed Electric field Treatment
PMT	Pulsed Magnetic field Treatment
EMCT	Electromagnetic Coupling Treatment
BM	Base Material
HAZ	Heat-affected Zone
FZ	Fusion Zone
SEM	Scanning Electron Microscope
EBSD	Electron Backscattered Diffraction
TEM	Transmission Electron Microscope
S-N curves	Stress-fatigue life (number of cycles) curves
HMR	Heterogenous Microstructure Region
KAM	Kernel Average Misorientation
RF	Recrystallized Fraction
LAGB	Low Angle Grain Boundaries
HAGB	High Angle Grain Boundaries
SADE	Selected Area of Electron Diffraction

1. Introduction

Titanium and titanium alloys have the advantages of low density, high strength, non-magnetic, corrosion resistant, etc. As structural materials, they are widely used in aerospace products, ships, vehicles, the chemical industry, biomedicine and other fields [1-3]. For high temperature structural components such as aeroengine casings, good fatigue performance is an important goal. In order to reduce the consumption of raw materials and reduce the weight of structural parts, the joining process used for key positions of aerospace components is often welding [4]. There are many welding methods for titanium alloys, such as friction stir welding [5], laser welding [6], tungsten inert gas welding [7], metal inert gas welding (MIG) [8] and electron beam welding (EBW) [9].

Compared with other welding methods, electron beam welding of titanium alloy has the following advantages [4, 10, 11]:

i) EBW has large power density, so that the heat is extremely concentrated.

ii) EBW has high penetration capacity therefore the welding seam has a large depth to

width ratio.

iii) The welding speed is fast, and the physical properties of the welded joints are of high quality.

iv) The total input heat is small, therefore welding residual stress and deformation is small and it is easy to achieve high precision welding.

Therefore, although electron beam welding equipment is relatively expensive and a vacuum chamber is required for welding [11], to obtain excellent welding joint performance, titanium alloy electron beam welding has been widely used in the aerospace industry. Among all kinds of mechanical properties, fatigue performance is undoubtedly an important evaluation index of aviation structural parts as it is related to the safety and service life of aircraft. Any change to the electron beam welding parameters of titanium alloy will lead to a change in the the welded joint shape and internal microstructure. Compared to other welding methods, electron beam welding has the advantages of large energy density, strong penetrating ability, fast welding speed, and high welding accuracy [12]. It is used in the manufacture of large parts and complex parts. Processing and other aspects showed unique advantages. However, welding is a kind of non-equilibrium process of rapid heating and solidification, and the welded joint has large non-uniformity, including many complex phase transitions, segregation, inclusions, and other defects [13]. In addition, the non-uniformity of the structure of the heat-affected zone of the welded joint is significant [14]. The existence of these defects and inhomogeneities has a great influence on the mechanical properties of the welded joints, especially the fatigue properties.

Field technology is an emerging technology in manufacturing, including magnetic fields, electric fields, microwave fields, ultrasonics, etc. It is often used in metallurgy and metal modification treatment, and has attracted widespread attention due to its rapid, low-temperature, and environmentally friendly characteristics [15]. After years of related research by domestic and foreign scholars, it has been found that the electromagnetic coupling external field enhancement processing technology has the following technical advantages [16-21]:

i) Promote the progress of the vacancy defects and atomic diffusion behavior in the

material, relaxes the peak stress, thereby slows down the crack initiation, and increases the fatigue life of the material.

ii) Activates the movement of the dislocation source, the dislocation density will increase sharply, and the displacement of the domain wall will effectively hinder the movement of the dislocations and cause the dislocation density to increase further and cause hardening.

iii) Changing the electronic configuration between the pinned object and the dislocation, causing the original low-energy stable state to change to a high-energy unstable state, and the dislocation is unpinned.

iv) Electromagnetic vibration generated by alternating positive and negative pulses of magnetism and electrostriction interacts with residual stress, regional dislocation slippage, plastic deformation, and reduction of residual stress.

In this study, in view of the urgent need to improve the fatigue performance of Ti2AlNb welded joints, the electromagnetic coupling external field strengthening technology was innovatively adopted to do the following. Promote the slip and proliferation of dislocations inside the material, improve plastic deformation and prevent the expansion of fatigue cracks to achieve the improvement of fatigue life, provide a new solution for improving the fatigue life of welding materials.

2. Materials and experimental procedures

2.1 Materials

The Ti_2AlNb based alloy used in this study was provided by the AVIC Manufacturing Technology Institute with nominal chemical composition given in Table 1 and the static mechanical properties are shown in Table 2. The material was welded into a test plate with length of 200mm, height of 68mm and thickness of 8.5mm and post-weld heat treatment (PWHT) was conducted on the material. The parameters of the electron beam welding and heat treatment process are listed in Table 3. Fig. 1 shows the dimensions of the plate. Specimens were obtained from the material plate by wire cut electrical discharge machining (WEDM).

Specimens were designed to be plate-shaped making sure the welding area is locating at the center of the specimen.

Table 1. Chemical composition of the material.

Name	Al	Nb	Mo	Ti
Percentage, wt%	22	24	0.5	Balance

Table 2. Static mechanical properties of Ti-22Al-24Nb-0.5Mo.

Yield strength, MPa	Ultimate strength, MPa	Fracture location
937	1095	FZ/HAZ

Table 3. Welding parameters of Ti_2AlNb material.

Accelerate voltage, kV	Focusing current, mA	Welding speed, mm/s	Electron beam, mA	Linear energy, J/mm	Heat treatment, °C	Holding time, h
120	43	20	1870	258	860	4

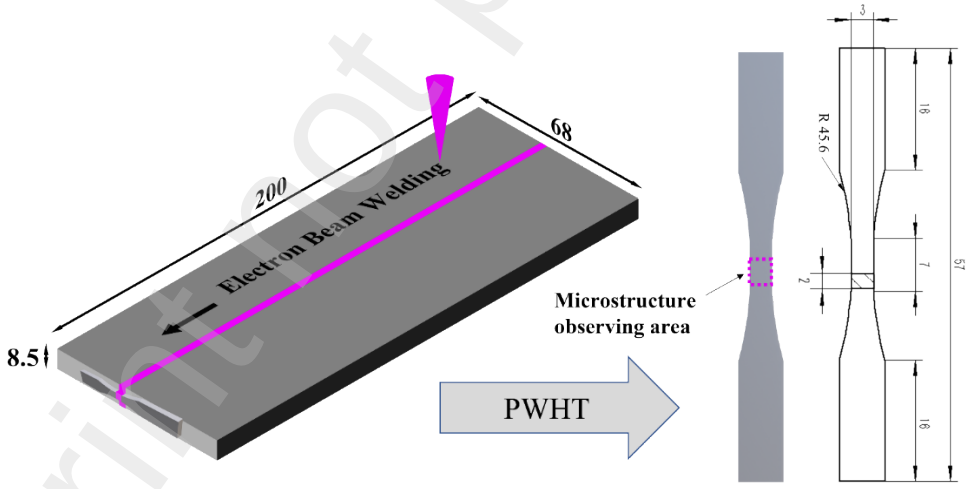

Fig. 1. Schematic diagram of sampling method and dimensions of fatigue specimen (unit in mm).

2.2 Pulsed electric field treatment (PET), Pulsed magnetic field treatment (PMT) and Electromagnetic coupling treatment (EMCT)

The samples to be treated were placed in the excitation coil working cavity of the self-designed electromagnetic coupling treatment (EMCT) device and pulsed electric field circuits

are connected on both sides of the welds. The working principle of the device has been reported in former studies [21]. Next, a pulsed electric field and pulsed magnetic field were applied to the welds by an electromagnetic coupling processing device as shown in Fig. 2. The voltage of the pulsed electric field was 0V and 1.0V, respectively. The intensity of pulsed magnetic field is 0T and 1.0T, respectively. There were 4 groups of different parameters, untreated (UT), pulsed electric field treatment (PET), pulsed magnetic field treatment (PMT) and electromagnetic coupling treatment (EMCT). The detailed parameters are listed in Table 4.

Table 4. Parameters of electromagnetic coupling treatment.

Group	Electric field, V	Peak current density, A/mm^2	Frequency, Hz	Number of times	Magnetic field, T	Interval, s	Number of times
UT	-	-	-	-	-	-	-
PET	1.0	10.67	50	150	-	-	-
PMT	-	-	-	-	1.0	10	20
EMCT	1.0	10.67	50	150	1.0	10	20

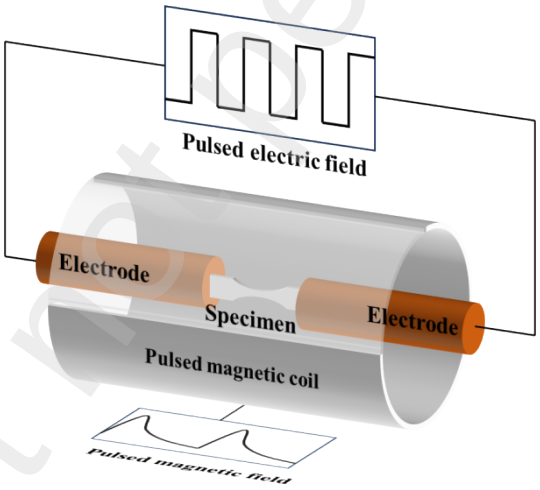

Fig. 2. Schematic diagram of the working zone.

2.3 Measurements

The WDW-RD100 testing machine (HST, China) was used to carry out constant amplitude tensile and compression cyclic fatigue tests on the samples before and after treatment at room temperature. All fatigue samples were polished to a mirror state (Ra = 0.2) to eliminate the influence of surface roughness on fatigue properties. The loading frequency is 15Hz, the

applied stress ratio R is -1, the stress load range is 400MPa to 700MPa, and the stress interval is 100MPa. An XL-640 X-ray diffraction system was used to measure the transverse residual stress distribution of the samples before and after EMCT by χ method. The test point was from the weld center to the HAZ with a distance of 1.5mm, as shown in Fig. 3. Each specimen is chemically polished to eliminate the effects of machining. The polishing liquid is composed of HF, HNO_3, H_2O_2, H_2O, and the volume ratio is 1:2:35:50. The fatigue crack growth rate of the three-point bending specimen shown in Fig. 4 was measured by an INSTRON 8801 hydraulic fatigue testing machine before and after EMCT. The microhardness of FZ, BM and HAZ samples before and after EMCT was measured by THVS-1M-AXYZM microhardness tester (LABTT, China). The load is set to 100g and the hold time is set to 10s.

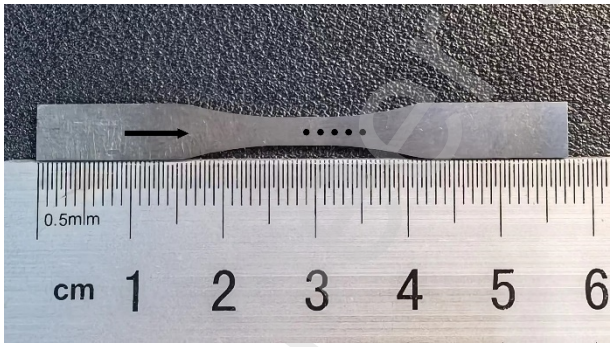

Fig. 3. Residual stress test point.

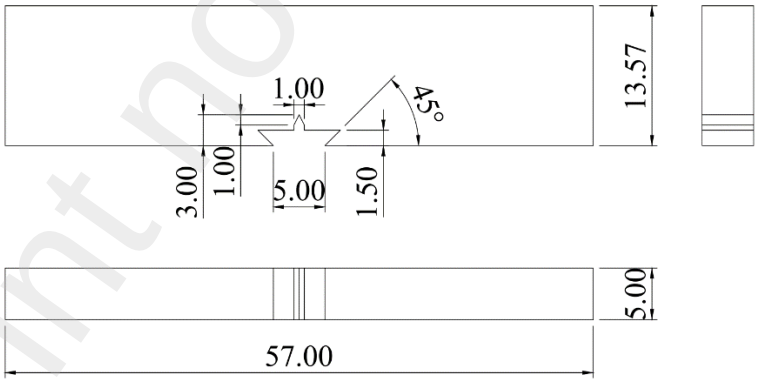

Fig. 4. Three-point bending sample.

The fatigue fracture, fatigue crack growth morphology and the microstructure of FZ and HAZ before and after EMCT were observed by an FEI Quanta 650F scanning electron microscope (FEI, US). Equipped with an Electron backscattered diffraction (EBSD) detector, the phase morphology and sizes were determined according to the EBSD scanning results

analyzed by HKL Channel 5 software. A Talos F200X transmission electron microscope (TEM) (FEI, US) was used to investigate the effects of EMCT on dislocations and deformation on the fusion zones and heat-affected zones of the welding area. The TEM samples were prepared by the focused ion beam (FIB) method via a Gatan 695 FIB instrument. The resolution of ion guns was 2.5 nm and it worked at 500 V–30 kV with beam of 1 pA-50 nA. The accelerating voltage of the field emission electron gun was 30 kV and its working distance was 9 mm. The sample preparation parameters are ion beam energy 5 Kev, ion gun angle ± 8° thinning to the hole; 4 Kev ± 4° thinning for 5min; 4 Kev ± 4° thinning for 5min; 3 Kev ± 3° thinning for 5min.

3. Results and discussion

3.1 Fatigue performance

A fatigue test was performed to decide the optimal EMCT parameters. Due to the limited numbers of specimens, each group of parameters were repeated at least twice, the results were showed in Table 5.

Table 5. Fatigue results of Ti2AlNb EBW joint with different treatments.

Treatment	Fatigue load, kN	Stress amplitude σ_a, MPa	Number	Fatigue life N_f, cycles
UT	4.2	700	UT-1	5227
			UT-2	1128
	3.6	600	UT-3	15168
			UT-4	11722
	3.0	500	UT-5	20601
			UT-6	31484
			UT-7	33985
	2.4	400	UT-8	97491
			UT-9	46428
			UT-10	137951
PET	4.2	700	PET-1	2226
			PET-2	1260
	3.6	600	PET-3	12865
			PET-4	9514
	3.0	500	PET-5	29514

			PET-6	20601
	2.4	400	PET-7	97491
			PET-8	74630
			PET-9	139595
	4.2	700	PMT-1	5227
			PMT-2	1177
			PMT-3	5219
	3.6	600	PMT-4	10286
			PMT-5	11408
PMT	3.0	500	PMT-6	33919
			PMT-7	22020
	2.4	400	PMT-8	147506
			PMT-9	98606
			PMT-10	69085
	4.2	700	EMCT-1	5644
			EMCT-2	5220
	3.6	600	EMCT-3	11039
			EMCT-4	14042
	3.0	500	EMCT-5	30189
EMCT			EMCT-6	49895
			EMCT-7	50380
	2.4	400	EMCT-8	83985
			EMCT-9	167918
			EMCT-10	181190

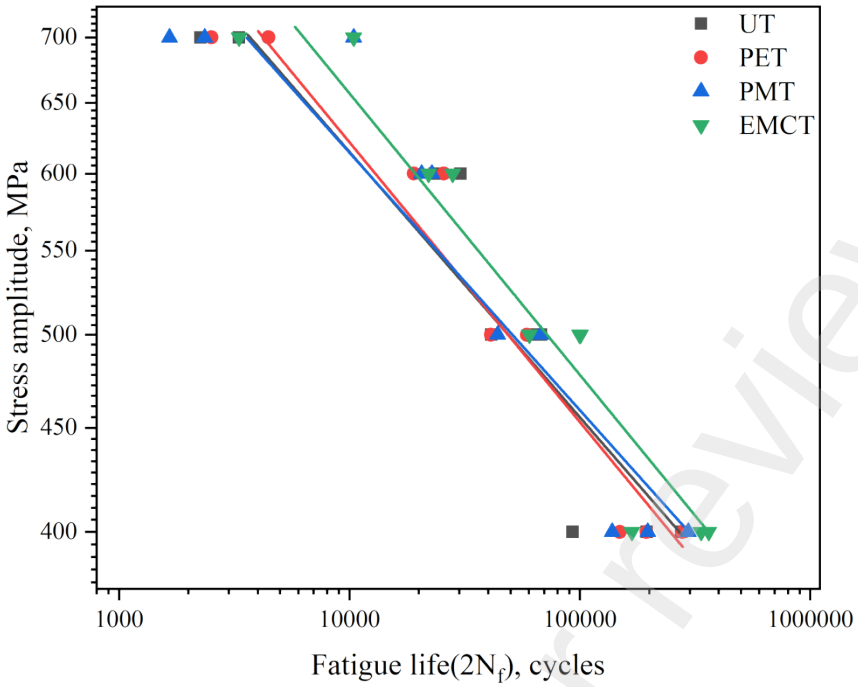

Fig. 3. S-N curve of the Ti_2AlNb EBW joints.

As Table 5 shows, all the EBW joints have a fatigue life between 10^3 and 10^5 cycles, which suggests that main fatigue failure mode of EBW joints is the fracture caused by crystallographic slip due to inner inhomogeneities of the microstructure. Stress amplitude versus fatigue life (S-N) curves for four groups of Ti_2AlNb EBW specimens are illustrated in Fig. 3, as demonstrated by a dark square, red circle, blue triangle and green nabla for UT, PET, PMT and EMCT, respectively. The linear fitting of Basquin's equation can be used to predict fatigue behavior in high cycle fatigue tests, representing in the following form [22]:

$$S = \sigma_f'(2N_f)^b \quad (1)$$

where S is the stress amplitude, N_f is number of cycles to failure, σ_f' is the fatigue strength coefficient and b is the Basquin exponent. The S-N curves of PET, PMT and UT are almost coincident with a slight variance, indicating that PET and PMT have no significant advantage on improving the fatigue limit of Ti_2AlNb EBW joints. Moreover, the S-N curve of EMCT is above the other curves, which shows that for Ti2AlNb EBW joints, EMCT is more advantageous on improving the fatigue limit than other treatments. It is worth pointing out that different linear fitting curves of Basquin's equation have similar slope values, in other words,

the values of the Basquin exponent are similar, that is to say, different treatment does not significantly change the shape of the S-N curves.

In this study, the fatigue life is considered as infinite when $N_f = 10^6$, by obtaining the value of σ'_f and b, the predicted fatigue limit $\sigma_{-1,10^6}$ (fatigue limit when R = -1, $N_f = 10^6$) can be calculated. According to equation (1), the value of σ'_f and b, the fatigue limits of the four groups of specimens were predicted as shown in Table 6.

Table 6. Parameters of linear fitting curves of Basquin's equation and predicted fatigue limits.

Group	σ'_f, MPa	b	$\sigma_{-1,10^6}$, MPa
UT	2.0417×10^3	-0.13046	307.6
PET	2.2082×10^3	-0.13758	299.9
PMT	1.9728×10^3	-0.12662	314.2
EMCT	2.3511×10^3	-0.13339	339.5

From Table 6, the predicted fatigue limit $\sigma_{-1,10^6}$ for UT group is 307.6MPa. Among three different treatment groups, EMCT has relatively the best performance, which improves the fatigue limit to 339.5MPa, increases 10.4%. For PET group, $\sigma_{-1,10^6}$ has dropped from 307.6 MPa to 299.9MPa, decreased 2%.

3.2 Residual Stress distribution

The samples were treated by EMCT. Fig. 5 shows the variation of the residual stress of the sample before and after EMCT, where "-" indicates that the residual stress is the residual compressive stress, and "+" indicates that the residual stress is the tensile stress. It can be seen from Fig. 5 that the residual stress of the welded joint before EMCT is basically the residual compressive stress, and its value ranges from 60 to 200MPa. The distribution of the residual stress decreases from the weld center to the base metal area, and the absolute value of the residual stress changes greatly. After EMCT, the residual compressive stress of most points of the sample was enhanced, while the change of a few points before and after EMCT was small, and the strengthening effect of residual stress was more significant in the center area of the weld.

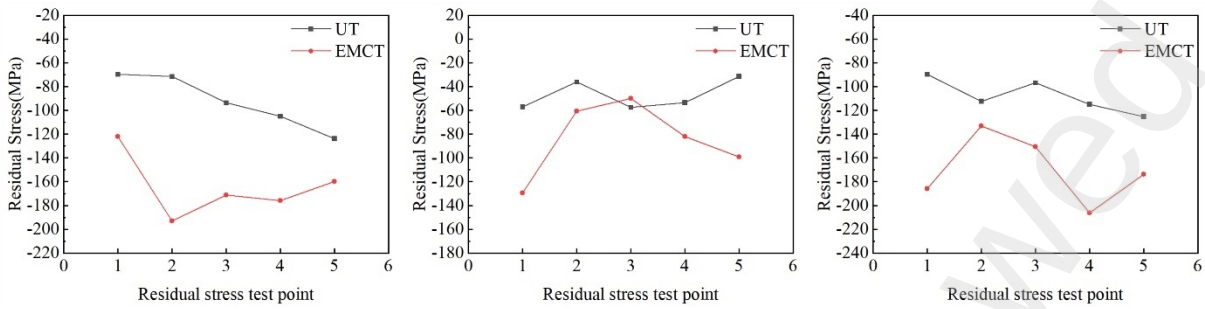

Fig. 5. Residual stress in the X direction after EMCT.

3.3 Fatigue crack growth

3.3.1 Closure effect of EMCT on microscopic cracks in Ti_2AlNb welded joints

Fig. 7(a) - (e) show the overall morphology of fatigue crack growth, the initial morphology of the main crack, the morphology of the crack growth zone, the main crack tip and the secondary crack tip of the untreated sample, respectively. With the increase of the number of fatigue load cycles, the width of the main crack decreases gradually, and nearby secondary cracks are gradually generated in parallel with the main crack. With the propagation of cracks, the number of secondary cracks increases gradually. The length of the initially fabricated main crack observed in the photo is 0.6mm, the length of the secondary crack is about 10μm, and the interval between the main crack is 2μm.

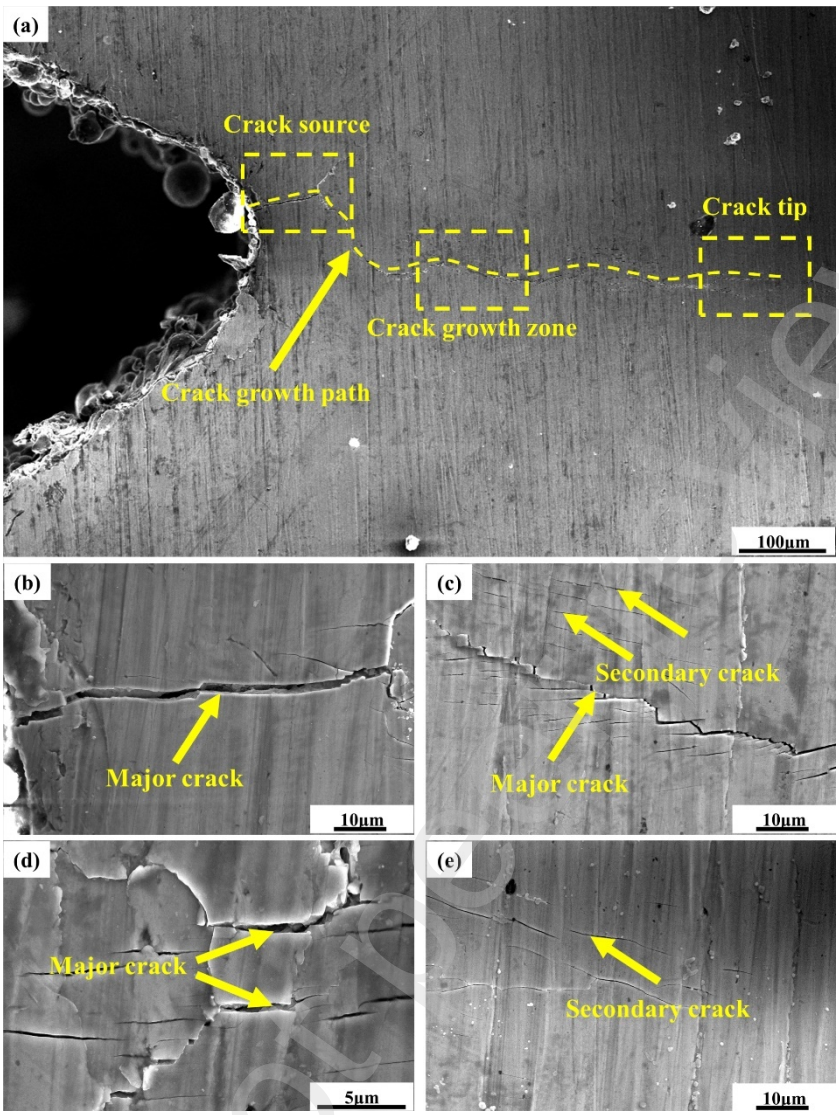

Fig. 7. Fatigue cracks of untreated specimens, (a) overall morphology, (b) initial crack growth morphology, (c) crack growth region morphology, (d) main crack tip and (e) secondary crack tip.

Fig. 8 shows the fatigue crack morphology of the sample after EMCT. At the main crack, a bridge structure was found in the middle of the crack, as shown in Fig. 8(b) and (c). Fig. 8(d) and (e) morphology of primary crack tip and secondary crack tip. Traces of crack closure were found at the tip of the main crack, while the secondary crack in Fig. 8(e) was completely closed, and small particles appeared on the surface of the crack, indicating that the crack produced local melting and resolidification, and oxidation occurred.

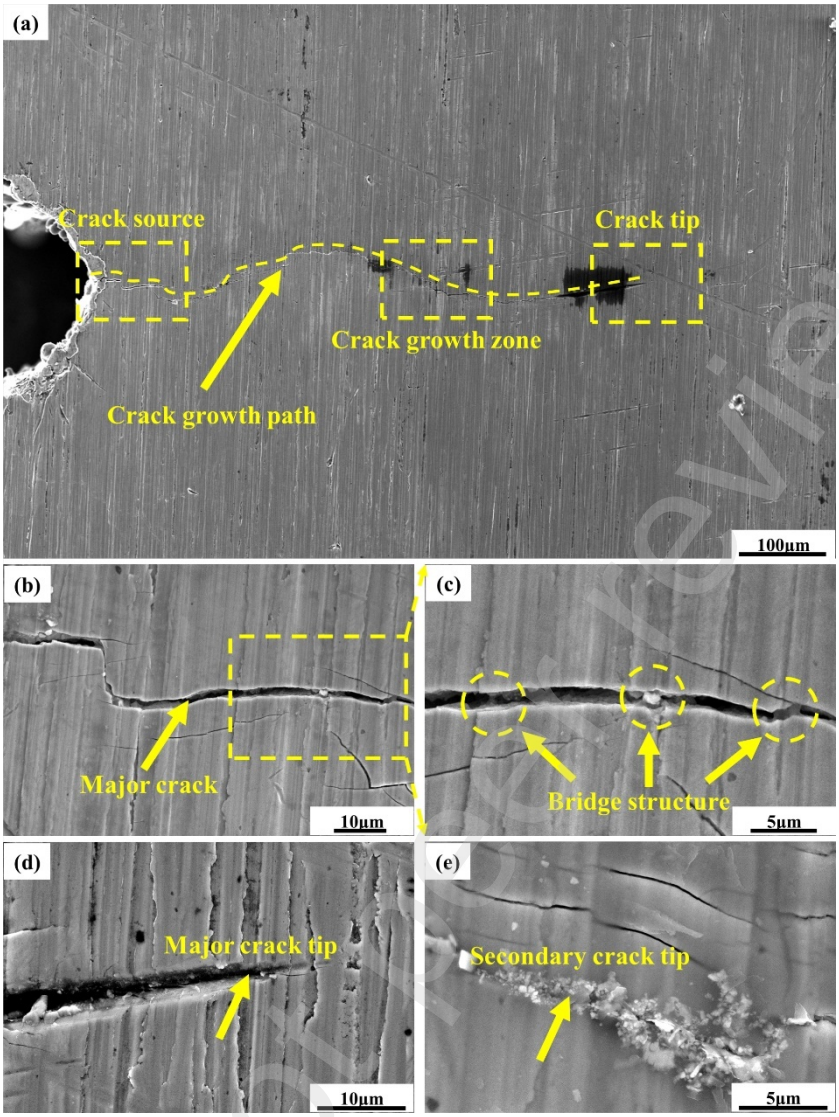

Fig. 8. Fatigue cracks of samples after EMCT, (a) overall morphology, (b) initial crack growth morphology, (c) crack growth region morphology, (d) main crack tip, (e) secondary crack tip.

The main reason for the above phenomenon is that the current flows around the crack tip, which makes the local current density at the crack tip significantly higher than that around the crack tip area. The Joule thermal effect generated by the local high density current induces the local melting of the crack tip, thus promoting the healing of the crack [23, 24]. At the same time, because the crack tip is restricted by the surrounding unheated area, the current will form a hot compression stress at the crack tip, which can seal the crack and hinder the crack expansion. Some studies have pointed out that excessive current density will cause thermal damage around cracks, thereby increasing local stress concentration and reducing fatigue life [24]. Under the condition of EMCT, no thermal damage phenomenon as mentioned in the

literature was observed, which indicates that the closure effect of EMCT is dominant at this time, which can delay fatigue crack propagation and improve fatigue life.

3.3.2 Effect of EMCT on fatigue crack propagation rate of Ti_2AlNb welded joint

Based on the initially fabricated crack, the cyclic stress is applied to the sample for a certain number of times, and then the crack length A is taken off and the operation is repeated until the sample is completely broken. Then the shape factor f and stress intensity factor amplitude ΔK are calculated to obtain the fatigue crack growth rate curve. The shape factor of SEN B3 sample is calculated as follows:

$$f = \frac{6a^{0.5}}{(1-2a)(1-a)^{1.5}}[1.99 - a(1-a)(2.15 - 3.93a + 2.7a^2)] \quad (2)$$

Where a is the crack length. The stress intensity factor amplitude K is calculated as shown in equation (3):

$$\Delta K = f\Delta\sigma\sqrt{\pi a} \quad (3)$$

Where f is the shape factor, Δσ is the stress amplitude, and a is the crack length.

Fig. 9 shows the fatigue crack growth rate curves of Ti_2AlNb welded joints before and after EMCT. It can be seen that the two da/dN-ΔK curves are approximately straight lines under the log-double axis, indicating that the measured data are all in the medium-speed crack growth zone, in line with the Paris relationship. The form of the Paris formula is [25]:

$$\frac{da}{dN} = C(\Delta K)^m \quad (4)$$

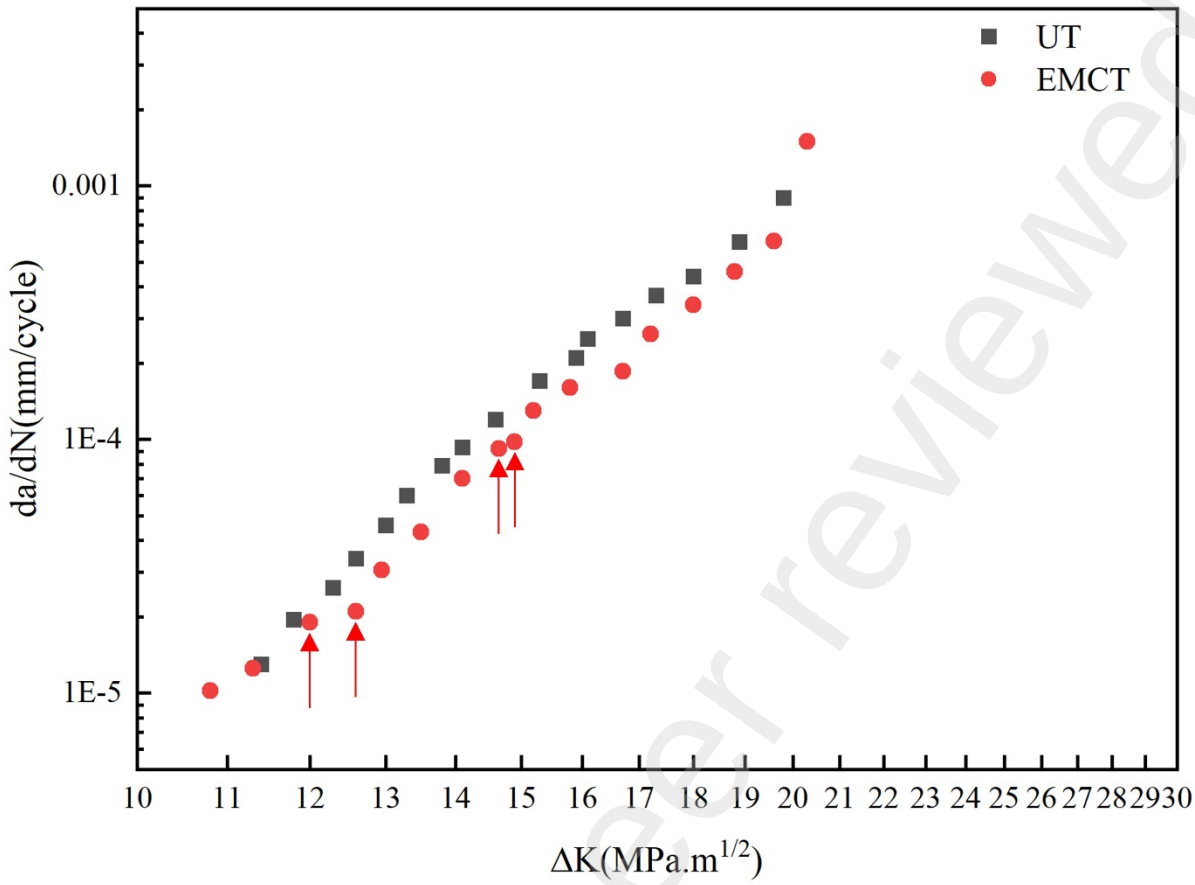

Fig. 9. da/dN-ΔK curves of Ti_2AlNb welded joint before and after EMCT.

Where a is the crack length, N is the number of stress cycles, C and m are material constants, and ΔK is the stress intensity factor amplitude. It can be seen from the figure that the initial crack growth rate is 10^{-5}mm/cycle, which is in the stage of low speed growth. With the increase of ΔK, the crack growth entered a stable stage. The da/dN-ΔK curve of the EMCT specimen is lower than that of the UT specimen, which indicates that the fatigue crack growth rate of the EMCT specimen is lower than that of the untreated specimen. At the same time, the da/dN-ΔK curve after EMCT has a delay of crack growth at the low-speed growth stage, which shows that the crack growth rate suddenly decreases, as shown by the arrow mark in the figure.

3.4 Fatigue Fracture Morphologies

The fracture morphologies of specimens with and without EMCT are shown in Fig. 10. It was observed that the fatigue crack of the UT sample initiated from the surface, but for the EMCT specimen the crack source located in the subsurface, as shown in Fig. 10(a) and (d). Also, an internal crack source which initiates at the grain boundary was observed in Fig 10(e).

The reason of this phenomenon can be explained by the increment of compressive residual stress on the surface. The surface residual compressive stresses make it more difficult to generate fatigue crack sources at the surface and this forces the crack sources to sprout inside the sample. However, on the subface, there were restrictions for the deformation, making the fatigue cracks initiate here difficult. Fig. 10(c) and (f) showed the fracture morphologies in crack propagation regions. It could be found that the density of fatigue striations in the EMCT sample was clearly higher than that in the UT sample, indicating the fatigue crack growing rate was effectively reduced by EMCT. Because of the presence of compressive residual stress, the nominal stress dropped as the fatigue fracture propagated, potentially reducing the fatigue crack development rate. When the fatigue crack propagates and expands, it will be blocked by the complex internal dislocation structures, for example, dislocation walls and dislocation tangles, which makes the expansion path of the fatigue crack more complicated. As Fig. 10(c) and (f) indicates, secondary cracks are observed in the UT sample while no obvious secondary cracks are found in the EMCT sample, and the crack striation propagates in different directions. Also, the fatigue crack propagating rate was also reduced because of the healing effects of microscopic cracks caused by compressive residual stress [26].

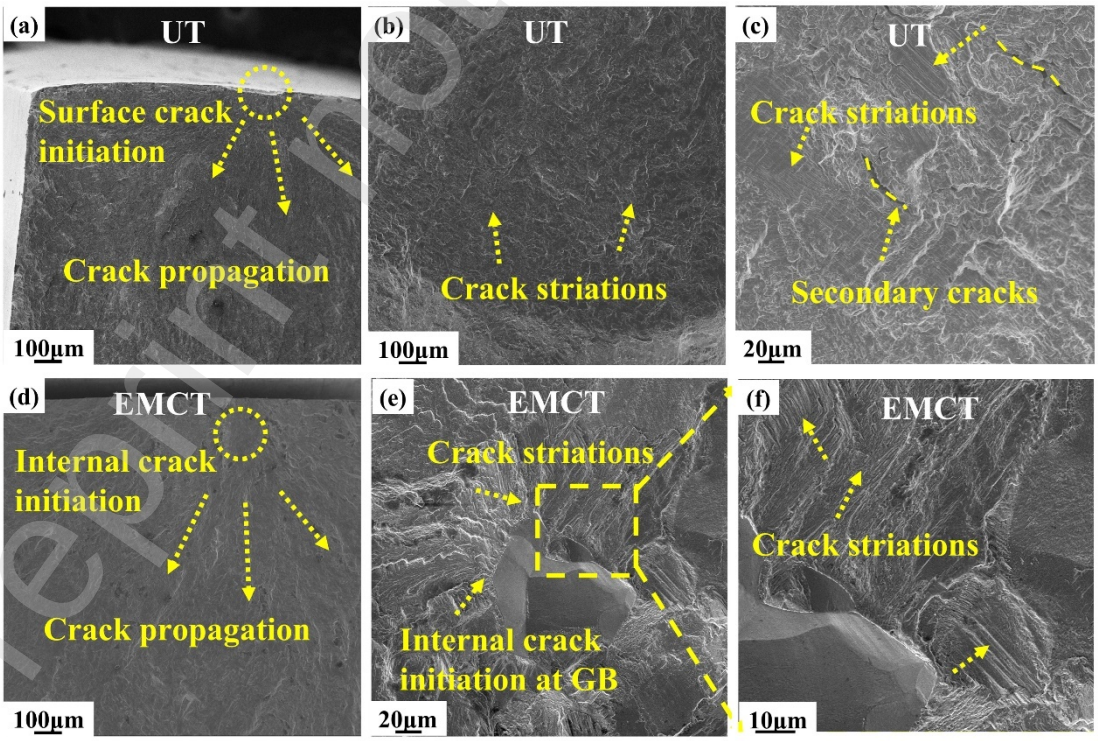

Fig. 10. Fracture image with and without EMCT, (a) - (c) are the fractures of UT-10 (σ_a = 400MPa, N_f = 137951), (d)-(f) are the fractures of EMCT-10 (σ_a = 400MPa, N_f = 181190).

3.5 Microstructure observations under SEM

Fig. 11 demonstrates the microstructure of the EBW joint without EMCT. As can be seen in Fig.11(a), the overall width of the weld is about 4.5mm, and there is an obvious boundary between the FZ and HAZ. The width of the FZ is about 2.5mm, and the epitaxial growth characteristics of the boundary of the FZ can be observed [27]. The FZ mainly consists of equiaxed and columnar grains, and the grain size is relatively large with an average diameter around 100μm. According to Fig. 11(b) and (d), O phase and B_2 phase form a basket-weave structure, in which the dark grey phase is O phase and the bright one is B_2 phase. The average size of O phase is around 1-2μm, as Fig. 11(d) indicates. The orientation of the cellular grains at the beginning of crystallization is approximately vertical to the edge of the FZ. When it grows to a certain stage, the growth direction of the cellular grains is affected by the direction of heat flow [28]. Driven by the heat flow in EBW joint, columnar grains gradually becomeequiaxed grains in the end of the FZ. In the HAZ, as Fig. 11(c) and (e) demonstrates, equiaxed microstructure dominates the area, α_2 phase, lamellar primary O phase slats and secondary O phase slats exist simultaneously. The size of secondary O phase slats is much smaller than that of primary O phase slats.

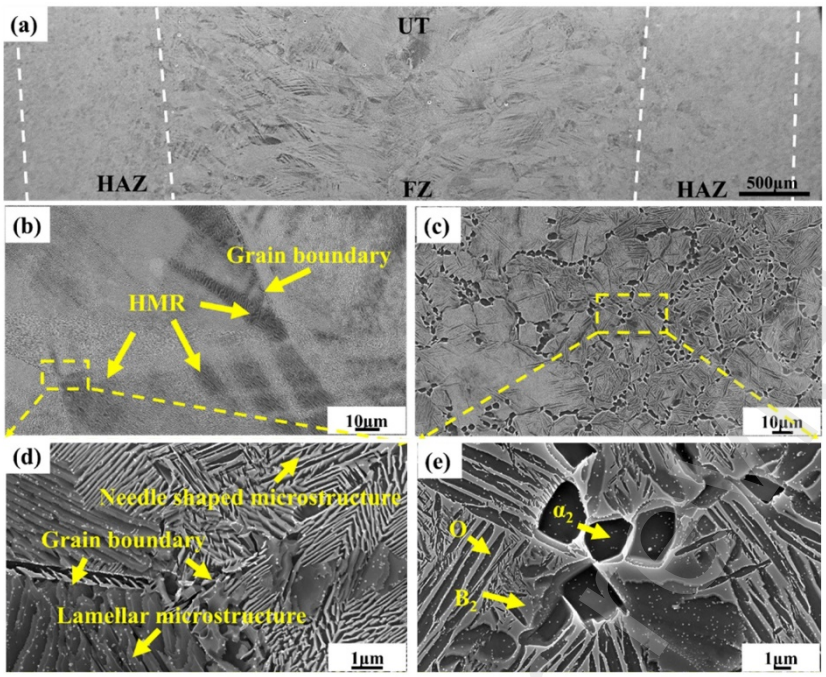

Fig. 11. Microstructure features in Ti_2AlNb EBW joint without EMCT, (a), macrostructure of FZ and HAZ, (b) - (c) low magnification image of FZ and HAZ, (d) – (e), high magnification image of FZ and HAZ.

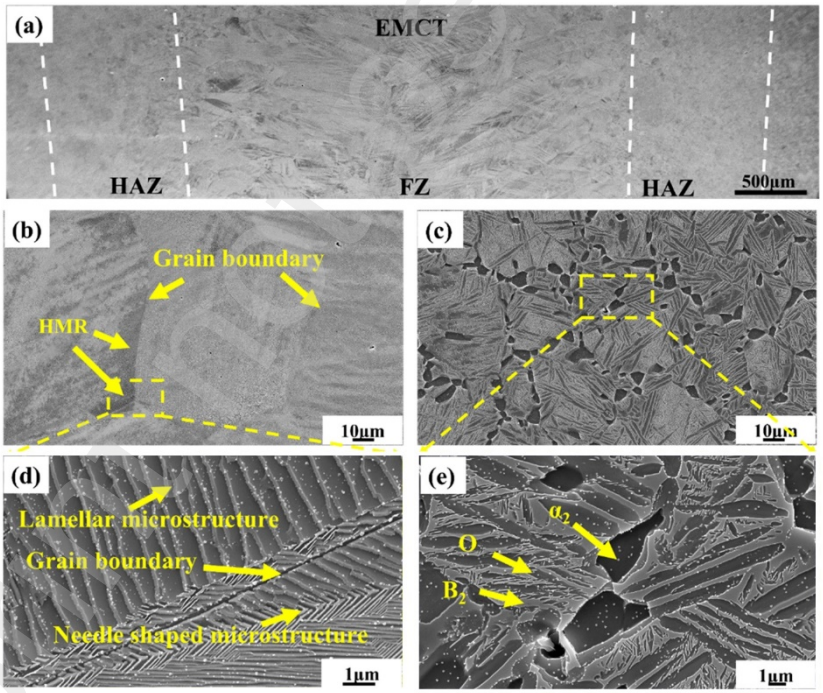

Fig. 12. Microstructure features in Ti_2AlNb EBW joint with EMCT, (a), macrostructure of FZ and HAZ, (b) – (c), low magnification image of FZ and HAZ, (d) – (e), high magnification image of FZ and HAZ.

It is worth pointing out that in FZ, heterogenous microstructure regions (HMR) are detected within a grain. The HMR consists of a needle shaped microstructure and lamellar

shaped microstructure, both these two microstructures are the form of O phase. HMR mainly occurs close to the grain boundary, which is believed to be the cause of stress concentration.

Image Pro Plus 6.0 image analysis software was used to compare the content of B_2 phase and O phase, and the results are shown in Table 7.

Table 7. Different contents of phase in FZ of EBW joint.

Group	O, %	B_2, %
UT	41.4	58.6
EMCT	42.7	57.3

The values of O phase and B_2 phase do not change prominently with and without EMCT, which is coincident with Fig. 11 and Fig. 12, there is no significant variation in the microstructure of EBW joint. This suggests that the coupling effects of the PWHT temperature and time play a dominant role in the forming mechanism of the microstructureand EMCT does not change the original metallographic characteristics of processed materials.

3.6 Microstructure evolution based on EBSD observations

Observations based on EBSD were conducted in order to obtain the changes of grain size and dislocations. The results are shown in Fig. 13 and Fig. 14.

The Kernel average misorientation (KAM) map is a method for describing local mean orientation deviations, and it is frequently used to describe dislocation density distribution in materials [29]. KAM distribution in the FZ before and after the EMCT are shown in Fig. 13(a), and (d), respectively. In the UT sample, the average misorientation angle density most frequently occurs at 0-1°, with a maximum relative frequency up to 1.69. Compared to the sample before EMCT, the most dense value of average misorientation angle increases to around 1° while relative frequency decreases to 1.0. This indicates that after EMCT, the KAM distribution of FZ is more uniform overall, suggesting that the dislocation density of the FZ is likewise uniform. The similar phenomenon occurs in the HAZ as well, as demonstrates in Fig. 13(a) and (d), the densest average misorientation angle increases from 0.6° to 0.9°, with respective relative frequency decreasing from 1.52 to 0.87. Also, in a sample before EMCT, at a region close to the grain boundary, the KAM density varies dramatically, this means the

dislocations are mainly located at the grain boundary. After EMCT, the difference of KAM distribution between grains and grain borders is less obvious, suggesting that the dislocations of the FZ might have climbed from grain boundaries to the intragranular position. The total dislocation density exhibits a homogeneity tendency, and the change in KAM distribution illustrates the dislocation density has been homogenized. It is hypothesized that this homogenization is due to the combination of dislocation stacking, generation, and annihilation, which may be confirmed by the fluctuation of GB angle.

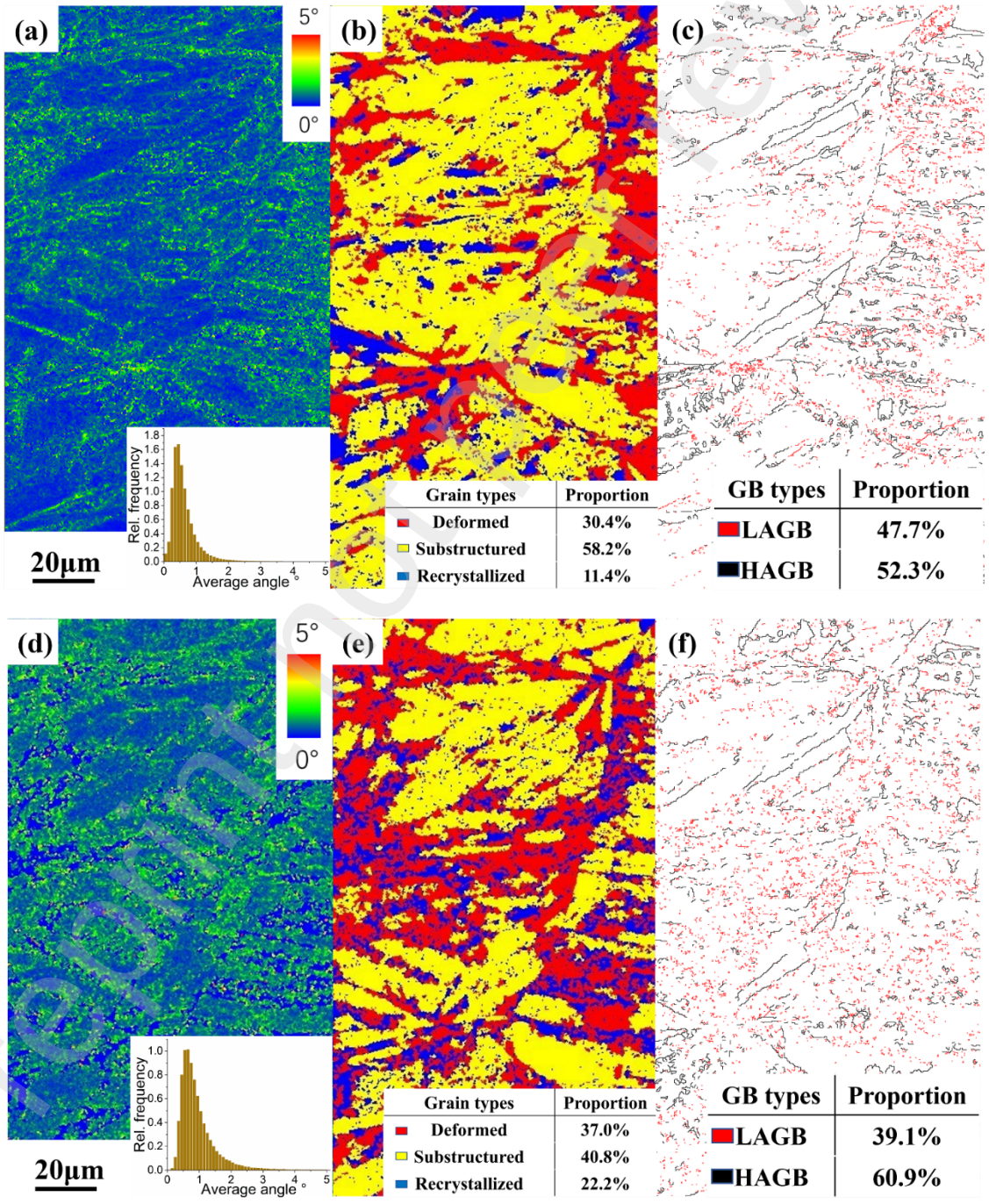

Fig. 13. Microstructure features in FZ before and after EMCT. (a), (b), (c); KAM, RF and GB map before EMCT, respectively; (d), (e), (f); KAM, Recrystallization fraction and GB map after EMCT, respectively.

Fig. 13(b), (e) represent the recrystallization fraction of FZ before and after EMCT. As shown in the figure, before the EMCT, the contents of deformed crystal, substructure crystal and recrystallization in the FZ are 30.4%, 58.2% and 11.4% respectively, while the contents of the deformed crystal, substructure crystal and recrystallization after the EMCT are 37.0, 40.8% and 22.2% respectively. Compared to the UT sample, after EMCT, the contents of deformed crystal and recrystallization both increases, while the content of substructure crystal decreases to 47.8%. It can also be seen from Fig. 13(c), (f) the fraction of low angle grain boundary (LAGB, 0-5°) in the FZ decreases from 47.7% to 39.1% while the fraction of high angle grain boundary (HAGB) increases from 52.3% to 60.9% in the EMCT sample, indicating that some LAGB has transformed to HAGB. It is worth pointing out that a substantial amount of LAGB appears in the intragranular area, and some of the original HAGB annihilates and disappears.

The increment of deformed grains may be owning to the Joule heating effect produced by the EMCT. The heat generated by the pulsed current introduces a certain amount of thermal compressive stress in the specimen joint, which is generated as the thermal expansion lags behind the temperature in the rapid heating process [30]. The thermal stress will cause a small amount of plastic deformation of the sample. This explains the increment of compressive residual stress. Such fluctuations of recrystallization content and GB fraction may be attributed to the dynamic recrystallization. The process of dynamic recrystallization is a combination of dislocation generation and annihilation, as discussed in KAM results. Dynamic recrystallization takes place primarily at the pre-existing grain boundaries in EMCT since new grain growth is more active along grain boundaries [31]. During this process, dislocations generated by EMCT accumulate progressively in LAGB, and when a critical value of the misorientation angle is achieved, LAGB will transform to HAGB. The plastic deformation introduces a large number of high-density dislocations within the intragranular area, which provides favorable conditions for recrystallization. It should be noted that the electron wind

effect causes dislocation changes and promotes the recrystallization process.The Joule heating effect does not generate enough thermal energy to heat the sample up to the recrystallization temperature, so it is the electron wind effect that causes dislocation changes and promotes the recrystallization process to occur [32].

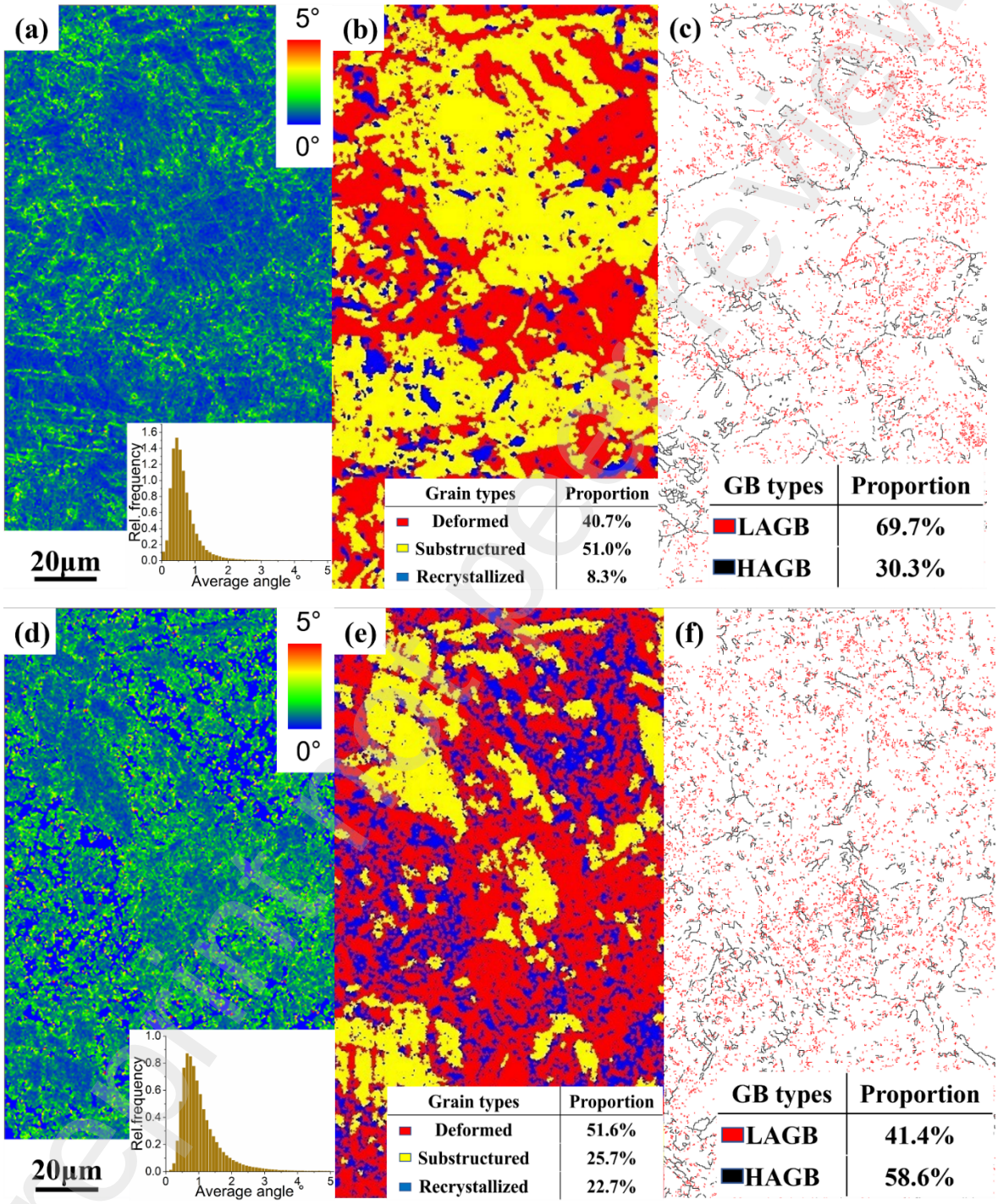

Fig. 14. Microstructure features in HAZ before and after EMCT. (a), (b), (c); KAM, RF and GB map before EMCT, respectively; (d), (e), (f); KAM, Recrystallization fraction and GB map after EMCT, respectively.

Fig. 14 demonstrates the KAM distribution, recrystallization fraction and GB distribution of the sample before and after EMCT in the HAZ. The variations of intergranular orientation in HAZ have the same trend as in the fusion zone, i.e., the homogenization of the KAM distribution, the increase in deformed and recrystallized grains, the decrease in substructure grain, and in LAGB. The reasons for these changes have been analyzed in the above section. In the HAZ, the content of deformed and recrystallized grains increases more significantly than in the FZ, this is because compared to the needle shaped microstructure in the FZ, the equiaxed microstructure of the HAZ is more sensitive to EMCT. Hence, the plastic deformation is more severe in HAZ, resulting in a higher fraction of deformed grains.

3.7 Dislocation evolution based on TEM observations

The TEM images in FZ of Ti_2AlNb weld joint with and without EMCT are demonstrated in Fig. 15. As demonstrated in Fig. 15(a) and (b), O phase laths and B_2 phases laths show an alternating distribution. Overall, the EMCT sample shows more dense dislocation motion and plastic deformation properties compared to the UT sample, which matches with the KAM results in the EBSD observations. Few dislocation tangles and features of slight plastic deformation are observed within the needle-shaped grains. In Fig. 15(b), a very low dislocation density is shown near the grain boundaries, this indicates a low degree of plastic deformation in the UT sample. In Fig. 15(c), the bright phase is B_2 phase, and the dark phase is O phase, which is confirmed by the electron diffraction in Fig. 15(c1) and (c2). Sub-grain boundaries and tangled dislocation cells are observed in the O phase. In contrast to Fig. 15(a), a higher dislocation density is shown in Fig. 15(d). In Fig. 15(e), the orientation of the fault shows a more pronounced consistency, while localized high density dislocations are generated within the grain. Dislocation tangles pile up near the faults and generate orthogonal dislocation cells. In Fig. 15(f), newly formed grain boundaries can be observed, and a large number of high-density dislocations are clustered and tangled here. The accumulation of dislocations at the grain boundaries resulted in an increase of the local strain, which is easy to become a nucleation site for dislocations [33], hence increases the degree of distortion near the grain boundaries and

promotes the transition from LAGB to HAGB. This is consistent with the GB distributions in the EBSD observation. Meanwhile, the emerging grain boundaries break up the large laths into smaller sizes, which helps to reduce the grain size. Smaller grain size is related to better mechanical performances, which could explain the improvement of fatigue lifetime.

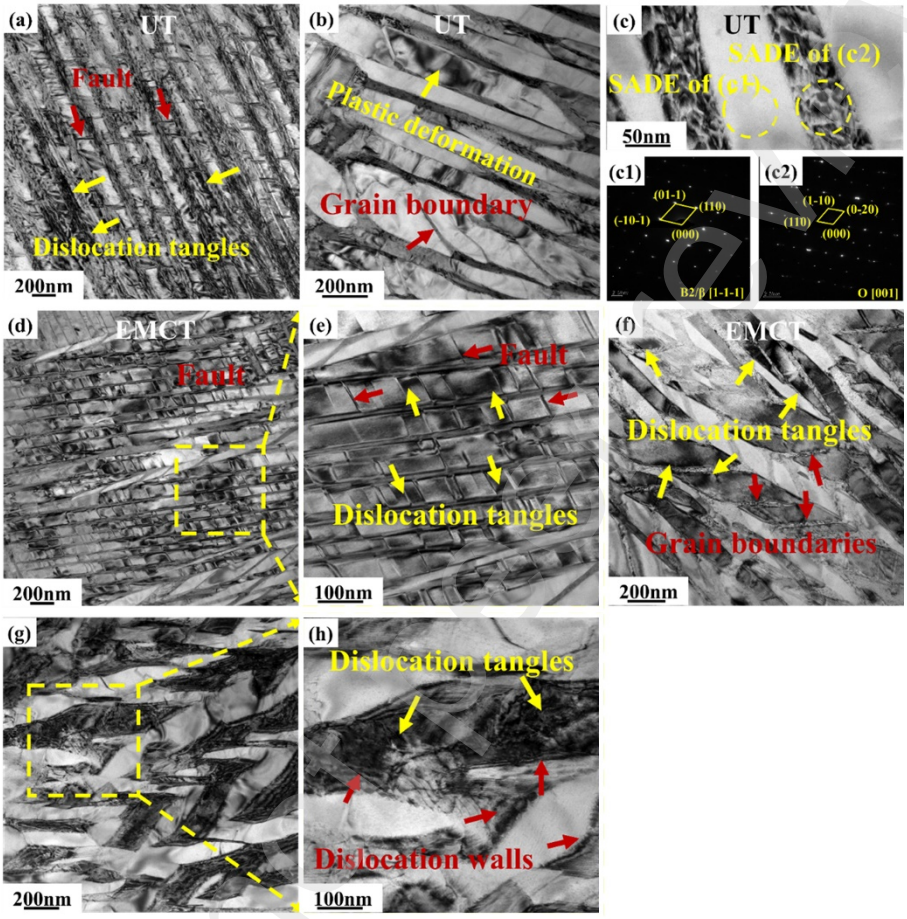

Fig. 15. Bright field TEM images in FZ of UT (a)-(c) and EMCT (d)-(h) Ti2AlNb EBW joint. (a)-(c) typical microstructure in UT sample. (c1) (c2) corresponding SADE pattern circled regions in (c). (d) Typical microstructure in EMCT sample. (e) Magnified image of selected region in (d). (f) Dislocation aggregation along grain boundaries. (g) Deformed structure features and high dense dislocations in EMCT sample. (h) Magnified image of selected region in (g) showing typical dislocation propagation.

The TEM images in HAZ of Ti_2AlNb welded joint with and without EMCT are demonstrated in Fig. 16. It was observed that there are almost no defects in HAZ, and the size of O phase laths were relatively smaller than in FZ. SADE patterns in Fig. 16(c1) and (c2)

indicate that micro-twins of O phase and B_2 phase are overlapping together, and dislocations cannot penetrate through the twin boundaries. Massive features of deformation including deformed needle-shaped grains and dislocation lines were found in Fig. 16(d) and (e). It is worth pointing out that a grain boundary acts as a source of dislocation emission. In Fig. 16(f), dislocation walls are generated at the boundary and transmitted along the O phase. It is worth pointing out that the interval of dislocation walls (marked by a yellow arrow) is much larger than its homolog (marked by red arrow). At the same time, the former has a severe deformation in the surrounding areas than the latter. According to grain boundary source theory [34], when large stress concentrations arise at grain boundaries, Frank-Read sources or nucleation sources are expected to operate preferentially at the boundary, which in this case, results in a higher dislocation density. In summary, EMCT makes it possible to promote more dislocation motion in the Ti_2AlNb EBW joint.

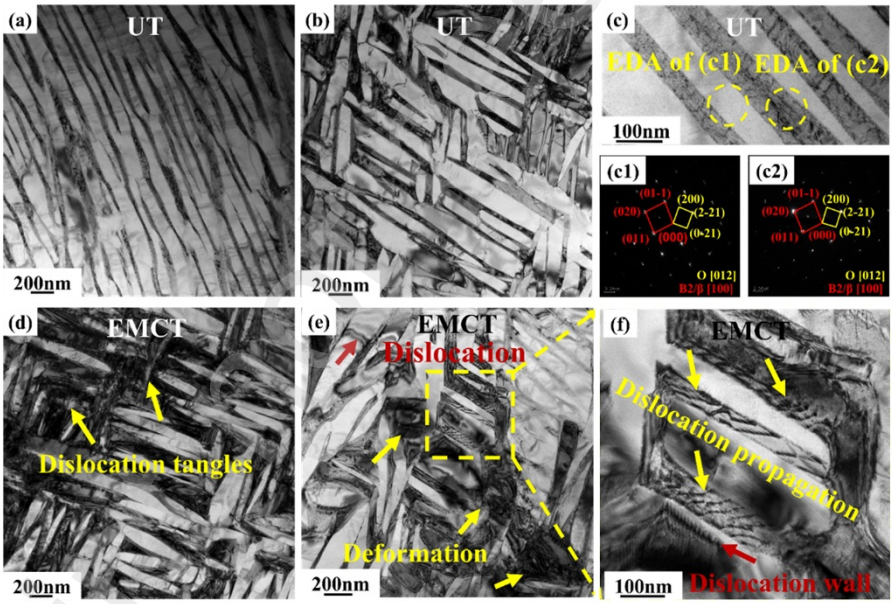

Fig. 16. Bright field TEM images in HAZ of UT (a)-(c) and EMCT (d)-(h) Ti2AlNb EBW joint. (a)-(c) typical microstructure in UT sample. (c1) (c2) corresponding SADE pattern of region in (c). (d) Typical microstructure in EMCT sample. (e) Deformed structure features and high dense dislocations in EMCT sample. (f) Magnified image of selected region in (e) showing typical dislocation propagation.

3.8 Micro hardness

The microhardness measurement results will change with the change of position, so

multiple points in different areas of the Ti_2AlNb welded joint were tested before and after EMCT, and the average hardness of different areas was calculated. Fig. 17 shows the average hardness changes in different areas of the Ti_2AlNb welded joint before and after EMCT. The hardness distribution of the Ti_2AlNb welded joint in different regions is very different. The basic law is that the hardness of the heat affected zone is the highest, followed by the fusion zone, and the hardness of the base material zone is the lowest. After EMCT, the average hardness of each area of the welded joint is higher than that of the UT.

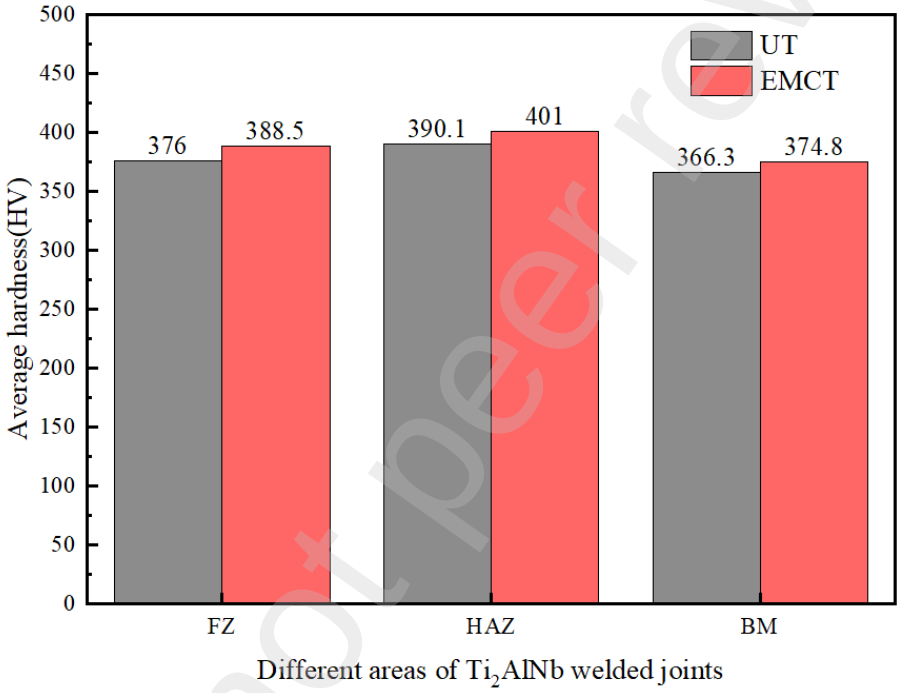

Fig. 17. Average hardness of Ti2AlNb EBW joint in FZ, HAZ and BM before and after EMCT.

The SEM results show that the grain size of the Ti2AlNb welded joint region is about 200μm, while the indentation size measured by microhardness is about 10μm. Therefore, it can be considered that the grain boundary has no significant influence on the hardness of the welded joint. It is inferred that the change of hardness of the Ti2AlNb welded joint is mainly due to the change of dislocation density. The results of EBSD and TEM show that the dislocation proliferation after EMCT causes a certain force on the lattice thus producing a slight distortion of the lattice. The Taylor relation [35] describes the action of the dislocation on the lattice, in the form:

$$\sigma = \alpha\mu b d^{1/2} \quad (5)$$

Where σ is the lattice stress, α is the dislocation action constant, μ is the shear modulus, b is the Boggs vector, and d is the dislocation density. The relationship between lattice stress and hardness can be expressed as follows [36, 37]:

$$HV = 3\sigma \quad (6)$$

Therefore, the relationship between hardness and dislocation density is:

$$HV = 3\alpha\mu b d^{1/2} \quad (7)$$

It can be seen from equation (7) that the hardness of the material is proportional to the square of the dislocation density. Therefore, it can be deduced that the change in the hardness of the Ti_2AlNb welded joint after EMCT is the result of the increase in dislocation density, and it also confirms that EMCT regulates the macro properties of the Ti_2AlNb welded joint by changing its microstructure.

3.9 Fatigue-life improvement mechanism with EMCT

The results from the examination of residual stress, microstructure, dislocation evaluation, and the improvement mechanism of fatigue life of a Ti2AlNb EBW joint have been thoroughly discussed.. The following factors are key to the contribution of fatigue life improvement.

Initially, it was clear that after EMCT, the compressive residual stress on the surface of Ti_2AlNb EBW joint is increased, this is due to the Joule heating effect during EMCT. The temperature increase of the sample by the Joule heating effect is estimated by the following equation:

$$\Delta T = \frac{\rho \int I^2 dt}{C_p d} \quad (8)$$

where ΔT is the maximum temperature rise, C_p = 0.612 kJ/kg is the specific heat of the specimen, $d = 4.51 \times 10^3$ kg/m^3 is the density of the specimen, $\rho = 1.686 \times 10^{-6}\ \Omega \cdot$ m is the resistivity of the specimen, $I = 10.33$A/cm^2 is the current density passing through the specimen. Based on this equation, the temperature increment can be calculated, as $\Delta T \approx 168.2$℃。 The thermal stress is calculated by the equation:

$$\sigma = E\alpha\Delta T \tag{9}$$

where E is the Young's modulus of the specimen, α is the coefficient of thermal expansion of the specimen and ΔT is the temperature increment. Based on equation (8) and equation (9), the theoretical thermal stress is around 136MPa. The enhancement of compressive residual stress significantly increases the resistance of micro crack initiation and forces the cracks to emerge in the subsurface layer..

There are many kinds of slip systems in the welded joints under different post-weld heat treatment temperatures. Under the action of a pulsed electric field, the free electrons in the crystal will be subjected to the action of an electric field force, resulting in drift, the so-called "electron wind" effect. According to the formula [32]:

$$\frac{\mathrm{f}_{ew}}{l} = \frac{bC_{ed}J}{M} \tag{10}$$

when Burger's vector of the dislocation in the welded joint is parallel to the drift direction of the electron, the electron will promote the slip system in a specific direction by the action of the electron wind force, so that the grain will have a small twist.

Under the action of a pulsed electric field, a large number of dislocations move. When their motion reaches a certain extent, such as perpendicular to the action direction of electron wind force, the pinning effect of dislocation will stabilize their motion. This makes the power/energy required for dislocation motion increase exponentially. Under the action of the pulsed magnetic field, when the magnetic moment direction of the electron is not in the same line with the direction of the external magnetic field, according to the Larmor precession frequency formula

$$\omega_{\mathrm{p}} = \frac{\mu g B}{h} \tag{11}$$

the spin state of the electron pair at the dislocation pin is changed by the Larmor precession frequency difference. Therefore, it is easier for the electron pair to enter and remain excited for a long time, this increases the energy and reduces the stability of the system. In this way, the electron pair energy state at the dislocation pinning site will be kept in an excited state with a greater probability, so that the dislocation is more likely to detach and move under the action of the electron wind force exerted by the pulse electric field.

The mechanism of EMCT to improve the fatigue performance of the Ti_2AlNb welded joint is shown in Fig. 18. The plastic deformation generated by thermal stress acts as a new source of dislocations generating a large number of intragranular dislocations. The electron wind force generated by the electric field provides sufficient momentum and the action of the magnetic field excites the free electrons within the atoms to raise them to excited states, thus making it easier for dislocations to move under the action of the original force field. The generation and annihilation of dislocations, the thermoplastic deformation, and the dynamic recovery and recrystallization occur simultaneously under the action of electromagnetic coupling treatment This ultimately results in generation of residual compressive stresses and improvement ofthe fatigue life.

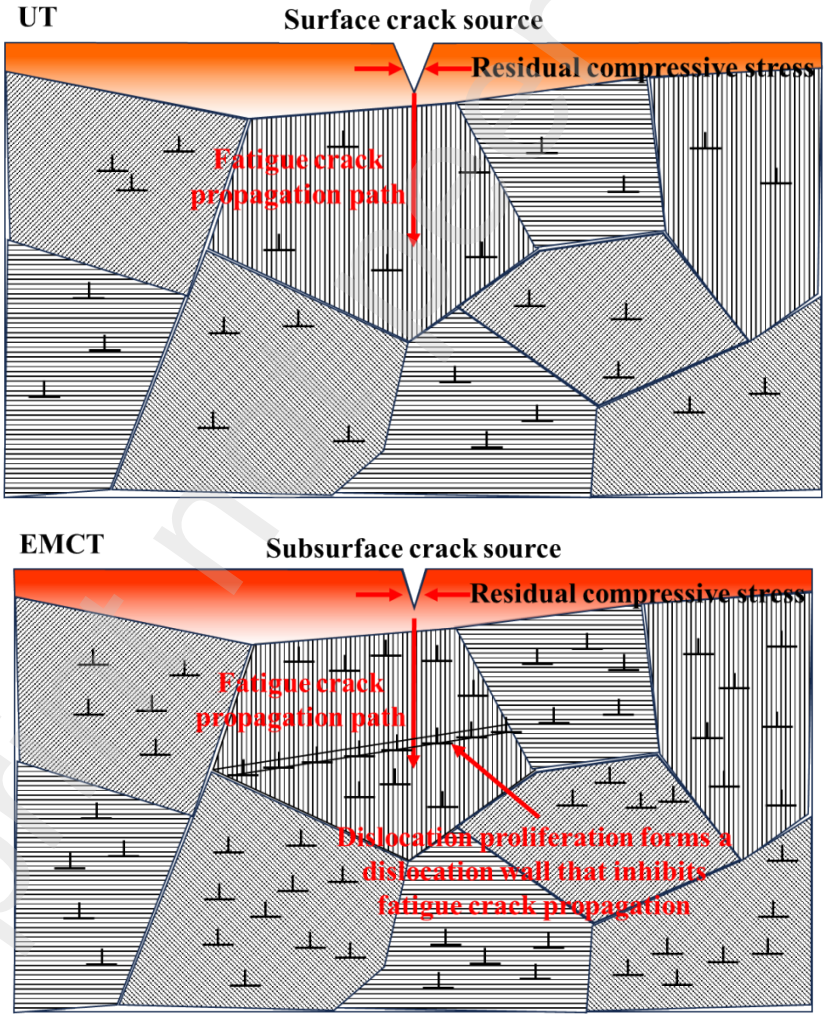

Fig. 18. Schematic diagram of the mechanism of EMCT.

4. Conclusions

In this study, the influence of EMCT on the fatigue properties of a Ti_2AlNb EBW joint was studied, the microstructure evolution was analyzed, and the mechanism of improving fatigue properties was put forward. The conclusion is as follows:

i) Compared to PET and PMT, the effect of EMCT on fatigue performance is more significant. Compared with UT specimens, the fatigue limit was increased by 10.4%.

ii) After EMCT, the compressive stress in the weld zone of the EBW joint increases and the fatigue crack propagation rate decreases.

iii) The Joule heating effect causes thermal stress in the weld zone, which causes plastic deformation and high-density dislocations, which depress the extension and expansion of micro cracks.

iv) Plastic deformation can form a new source of dislocation and produce a large number of intracrystalline dislocations, these provide power for dynamic recrystallization. Under the excitation of electron wind and magnetic field, dislocation is more likely to move, so that the dislocation density distribution is more uniform.

v) After EMCT, Joule thermal effect, thermoplastic deformation, dislocation generation and elimination, and dynamic recovery and recrystallization all occur simultaneously, resulting in the generation of residual compressive stress and the improvement of fatigue life.

Acknowledgments

The authors wish to acknowledge the financial support by the Sichuan Science and Technology Program (No. 2021ZDZX0001 and 2021ZDZX0002) and the Science Foundation of Zigong Government and Sichuan University (No. 2022CDZG-15). We would like to appreciate the Analytical and Testing Center of Sichuan University for structural characterization work, and we would be grateful to Yong Liu for her help with SEM analysis.

References

[1] T. Pasang, A.S. Budiman, J.C. Wang, C.P. Jiang, R. Boyer, J. Williams, W.Z. Misiolek, Additive

manufacturing of titanium alloys – Enabling re-manufacturing of aerospace and biomedical components, MICROELECTRON ENG, 270(2023) 111935. https://doi.org/10.1016/j.mee.2022.111935.

[2] P. Pushp, S.M. Dasharath, C. Arati, Classification and applications of titanium and its alloys, Materials Today: Proceedings, 54(2022) 537-542. https://doi.org/10.1016/j.matpr.2022.01.008.

[3] X. Han, J. Ma, A. Tian, Y. Wang, Y. Li, B. Dong, X. Tong, X. Ma, Surface modification techniques of titanium and titanium alloys for biomedical orthopaedics applications: A review, Colloids and Surfaces B: Biointerfaces, 227(2023) 113339. https://doi.org/10.1016/j.colsurfb.2023.113339.

[4] X. Liu, Q. Dong, P. Wang, H. Chen, Review of Electron Beam Welding Technology in Space Environment, OPTIK, 225(2021) 165720. https://doi.org/10.1016/j.ijleo.2020.165720.

[5] K. Gangwar, M. Ramulu, Friction stir welding of titanium alloys: A review, MATER DESIGN, 141(2018) 230-255. https://doi.org/10.1016/j.matdes.2017.12.033.

[6] M.M. Quazi, M. Ishak, M.A. Fazal, A. Arslan, S. Rubaiee, A. Qaban, M.H. Aiman, T. Sultan, M.M. Ali, S.M. Manladan, Current research and development status of dissimilar materials laser welding of titanium and its alloys, Optics & Laser Technology, 126(2020) 106090. https://doi.org/10.1016/j.optlastec.2020.106090.

[7] S.R. Singh, P. Khanna, A-TIG (activated flux tungsten inert gas) welding: – A review, Materials Today: Proceedings, 44(2021) 808-820. https://doi.org/10.1016/j.matpr.2020.10.712.

[8] V. Dhinakaran, S.V. Shriragav, A. Fathima Yasin Fahmidha, M. Ravichandran, A review on the categorization of the welding process of pure titanium and its characterization, Materials Today: Proceedings, 27(2020) 742-747. https://doi.org/10.1016/j.matpr.2019.12.034.

[9] S.Q. Wang, W.Y. Li, K. Jing, X.Y. Zhang, D.L. Chen, Microstructural evolution and mechanical properties of electron beam welded dissimilar titanium alloy joints, Materials Science and Engineering: A, 697(2017) 224-232. https://doi.org/10.1016/j.msea.2017.05.028.

[10] I. Krivtsun, V. Korzhyk, V. Nesterenkov. Chapter 7 - Electron beam welding, Elsevier, 2023.

[11] J. Ma, Z. Wang, Z. Liu, H. Ji, X. Xia, C. Li, Z. Liu, Z. Zhang, J. Wu, Investigation on microstructure and mechanical properties of 160mm thick 316L stainless steel electron-beam-welded joint, FUSION ENG DES, 195(2023) 113973. https://doi.org/10.1016/j.fusengdes.2023.113973.

[12] Z. Sun, R. Karppi, The application of electron beam welding for the joining of dissimilar metals: an overview, J MATER PROCESS TECH, 59(1996) 257-267. https://doi.org/10.1016/0924-0136(95)02150-7.

[13] B. ZHANG, M. SHI, G. CHEN, J. FENG, Microstructure and defect of titanium alloy electron beam deep penetration welded joint, T NONFERR METAL SOC, 22(2012) 2633-2637. https://doi.org/10.1016/S1003-6326(11)61510-0.

[14] F. Liu, Y. Chen, J. Mai, C. Wang, Q. Wang, Y. Liu, Optimizing microstructure and mechanical properties of Ti-5Al-2Sn-2Zr-4Mo-4Cr alloy electron beam welded joint through post-weld heat treatment, Journal of Materials Research and Technology, 26(2023) 7052-7071. https://doi.org/10.1016/j.jmrt.2023.09.052.

[15] H. Li, L.F. Peng, B. Meng, Z.T. Xu, L.L. Wang, G. Ngaile, M.W. Fu, Energy field assisted metal forming: Current status, challenges and prospects, International Journal of Machine Tools and Manufacture, 192(2023) 104075. https://doi.org/10.1016/j.ijmachtools.2023.104075.

[16] G. Li, H. Wang, X. Yuan, Y. Zhao, Microstructure of nanometer Al2O3 particles reinforced aluminum matrix composites processed by high pulsed electromagnetic field, MATER LETT, 99(2013) 50-53. https://doi.org/10.1016/j.matlet.2013.02.089.

[17] C. Liang, K. Lin, The microstructure and property variations of metals induced by electric current treatment:

A review, MATER CHARACT, 145(2018) 545-555. https://doi.org/10.1016/j.matchar.2018.08.058.
[18] L. Ma, W. Zhao, Z. Liang, X. Wang, L. Xie, L. Jiao, T. Zhou, An investigation on the mechanical property changing mechanism of high speed steel by pulsed magnetic treatment, Materials Science and Engineering: A, 609(2014) 16-25. https://doi.org/10.1016/j.msea.2014.04.100.
[19] H. Xiao, S. Jiang, K. Zhang, Y. Jia, C. Shi, Z. Lu, J. Jiang, Optimizing the microstructure and mechanical properties of a cold-rolled Al – Mg – Li alloy via electropulsing assisted recrystallization annealing and ageing, J ALLOY COMPD, 814(2020) 152257. https://doi.org/10.1016/j.jallcom.2019.152257.
[20] J. Xu, L. Huang, Y. Xu, B. Xie, M. Zhao, H. Su, Y. Wang, J. Li, Effect of pulsed electromagnetic field treatment on dislocation evolution and subsequent artificial aging behavior of 2195 Al-Li alloy, MATER CHARACT, 187(2022) 111872. https://doi.org/10.1016/j.matchar.2022.111872.
[21] Q. Zhang, X. Wang, Y. Qin, G. He, S. Zhang, K. Huang, J. Wang, Improving thermal conductivity of a nickel-based alloy through advanced electromagnetic coupling treatment, Journal of Materials Research and Technology, 21(2022) 4708-4723. https://doi.org/10.1016/j.jmrt.2022.11.066.
[22] D. Rial, H. Kebir, E. Wintrebert, J. Roelandt, Multiaxial fatigue analysis of a metal flexible pipe, Materials & Design (1980-2015), 54(2014) 796-804. https://doi.org/10.1016/j.matdes.2013.08.105.
[23] A. Hosoi, T. Nagahama, Y. Ju, Fatigue crack healing by a controlled high density electric current field, Materials Science and Engineering: A, 533(2012) 38-42. https://doi.org/10.1016/j.msea.2011.11.024.
[24] J. Jung, Y. Ju, Y. Morita, Y. Toku, Enhancement of fatigue life of aluminum alloy affected by the density of pulsed electric current, INT J FATIGUE, 103(2017) 419-425. https://doi.org/10.1016/j.ijfatigue.2017.06.021.
[25] Y. Liu, Y. Li, H. Chen, Z. Zhu, Fatigue crack propagation characteristics of aluminum/steel laser-metal inert gas fusion-brazed joints in different micro-zones, INT J FATIGUE, 183(2024) 108261. https://doi.org/10.1016/j.ijfatigue.2024.108261.
[26] A. Kumar, S.K. Paul, Healing of fatigue crack in steel with the application of pulsed electric current, MATERIALIA, 14(2020) 100906. https://doi.org/10.1016/j.mtla.2020.100906.
[27] R.H. Buzolin, T. Richter, F. Pixner, M. Rhode, D. Schroepfer, N. Enzinger, Microstructure characterisation of multi-principal element alloys welds produced by electron beam welding, MATER DESIGN, 225(2023) 111609. https://doi.org/10.1016/j.matdes.2023.111609.
[28] W. Chen, Z.Y. Chen, C.C. Wu, J.W. Li, Z.Y. Tang, Q.J. Wang, The effect of annealing on microstructure and tensile properties of Ti – 22Al – 25Nb electron beam weld joint, INTERMETALLICS, 75(2016) 8-14. https://doi.org/10.1016/j.intermet.2016.02.006.
[29] F. Liu, Y. Chen, C. He, C. Wang, L. Li, Y. Liu, Q. Wang, Very long life fatigue failure mechanism of electron beam welded joint for titanium alloy at elevated temperature, INT J FATIGUE, 152(2021) 106446. https://doi.org/10.1016/j.ijfatigue.2021.106446.
[30] J.B. Gao, D.D. Ben, H.J. Yang, L.X. Meng, H.B. Ji, D.L. Lian, J. Chen, J.L. Yi, L. Wang, P. Li, Z.F. Zhang, Effects of electropulsing on the microstructure and microhardness of a selective laser melted Ti6Al4V alloy, J ALLOY COMPD, 875(2021) 160044. https://doi.org/10.1016/j.jallcom.2021.160044.
[31] D. Ponge, G. Gottstein, Necklace formation during dynamic recrystallization: Mechanisms and impact on flow behavior, ACTA MATER, 46(1997) 69-80. https://doi.org/10.1016/S1359-6454(97)00233-4.
[32] H. Zhang, X. Zhang, Uniform texture in Al-Zn-Mg alloys using a coupled force field of electron wind and external load, J MATER SCI TECHNOL, 36(2020) 149-159. https://doi.org/10.1016/j.jmst.2019.07.025.
[33] H. Zhang, Z. Ren, J. Liu, J. Zhao, Z. Liu, D. Lin, R. Zhang, M.J. Graber, N.K. Thomas, Z.D. Kerek, G.

Wang, Y. Dong, C. Ye, Microstructure evolution and electroplasticity in Ti64 subjected to electropulsing-assisted laser shock peening, J ALLOY COMPD, 802(2019) 573-582. https://doi.org/10.1016/j.jallcom.2019.06.156.

[34] A.H. Cottrell, Theory of dislocations, Progress in Metal Physics, 1(1949) 77-126.

[35] Taylor, I. G., The Mechanism of Plastic Deformation of Crystals. Part I. Theoretical, Proceedings of The Royal Society A, 145(1934) 362-387.

[36] W.J. Poole, M.F. Ashby, N.A. Fleck, Micro-hardness of annealed and work-hardened copper polycrystals, SCRIPTA MATER, 34(1996) 559-564. https://doi.org/10.1016/1359-6462(95)00524-2.

[37] C. Shu, C. Liang, K. Lin, Electro-work hardening of metals induced by the athermal electromigration effect, Materials Science and Engineering: A, 772(2020) 138689. https://doi.org/10.1016/j.msea.2019.138689.